

Direct extraction of nuclear effects in quasielastic scattering on carbon

Callum Wilkinson¹ and Kevin S. McFarland²

¹*University of Bern, Albert Einstein Center for Fundamental Physics,
Laboratory for High Energy Physics (LHEP), Bern, Switzerland*

²*University of Rochester, Department of Physics and Astronomy, Rochester, New York 14627 USA
(Dated: December 3, 2024)*

The differences between neutrino and antineutrino CCQE cross sections measured on hydrocarbon targets are due to fundamental differences in the cross section, different neutrino and antineutrino fluxes from the same beamline, and the additional interactions on hydrogen for antineutrinos that are absent for neutrinos. In this analysis we correct for the former two differences to extract a constraint on the ratio of the CCQE cross section for free and bound protons from MINER ν A and MiniBooNE data. This measures nuclear effects in carbon, and we compare this measurement to models.

The cross sections for neutrino and antineutrino charged current quasielastic (CCQE) reactions on free nucleons, $\nu_\ell n \rightarrow \ell^- p$ and $\bar{\nu}_\ell p \rightarrow \ell^+ n$, can be expressed in terms of nucleon form factors [1–4]. This prescription, with form factors constrained by electron nucleon elastic scattering and pion electroproduction data, accurately describes available neutrino interaction data on hydrogen and loosely bound deuterium targets [5–9]. On heavier, more tightly bound nuclei, the relativistic Fermi Gas (FG) model [10] modifies this formalism within the context of the impulse approximation to include a simple description of the initial state of bound nucleons within the nucleus, and has been extensively used in neutrino interaction generators. However, experiments with carbon, oxygen and iron targets [11–19] with neutrino energies of a few GeV have measured a significantly different, typically higher, cross section than predicted by the FG model.

Theoretical work to understand these differences have been focused on three broad areas: a more sophisticated description of the initial state of nucleons within the nucleus [20–27]; contributions to the cross section beyond the impulse approximation which involve multiple initial state nucleons (hereafter referred to as multinucleon processes or MNP) [28, 29]; and collective effects which modify the cross section, which are generally referred to by the name of the calculation, the Random Phase Approximation (RPA) [28, 29]. Despite the flurry of theoretical activity in recent years, a consistent picture has yet to emerge, in part because of significant differences in the predictions of theoretical calculations [30–32].

Quasielastic interactions are especially important for accelerator neutrino oscillation experiments at GeV energies [33–37]. In the impulse approximation, the initial state nucleons are independent in the mean field of the nucleus, and therefore the neutrino energy and momentum transfer Q^2 can be estimated from the polar angle θ_ℓ and momentum p_ℓ of the final state lepton. However, the initial state prescription and multinucleon processes both disrupt this relationship in different ways [38–40]. MNP and collective RPA processes both alter the distribution

of Q^2 which can in turn alter the relative acceptance of near and far detectors. Therefore understanding nuclear modifications is essential for the current and future generations of neutrino oscillation experiments.

In this analysis, we present a method for extracting a measurement of the suppression to the CCQE cross section due to nuclear effects in carbon from neutrino and antineutrino measurements on hydrocarbon targets. This method is largely model independent when applied to high energy CCQE data, such as that from MINER ν A [15, 16], but less so at the lower energies of the MiniBooNE experiment [11, 17].

The CCQE neutrino–nucleon differential cross section for free nucleons as a function of the negative of the four-momentum transfer squared, Q^2 , can be expressed using the Llewellyn-Smith formula [4]:

$$\frac{d\sigma}{dQ^2} \left(\begin{array}{l} \nu_\ell n \rightarrow \ell^- p \\ \bar{\nu}_\ell p \rightarrow \ell^+ n \end{array} \right) = \frac{M^2 G_F^2 \cos^2 \vartheta_C}{8\pi E_\nu^2} \quad (1)$$

$$\times \left[A(Q^2) \pm B'(Q^2) \frac{(s-u)}{M^4} + C(Q^2) \frac{(s-u)^2}{M^4} \right],$$

where M is the mass of the struck nucleon, G_F is Fermi's constant, ϑ_C is the Cabibbo angle, E_ν is the incoming neutrino energy and s and u are the Mandelstam variables. $A(Q^2)$, $B'(Q^2)$ and $C(Q^2)$ are functions of the vector form factors: $F_V^{1,2}$, constrained by electron nucleon elastic scattering experiments [5, 7]; the axial form factor, F_A , constrained by neutrino scattering experiments on hydrogen and deuterium and from pion electroproduction [6–9]; and the pseudoscalar form factor, F_P , which is derived from F_A [4]. Uncertainties from F_P and the assumption that second class currents can be neglected are discussed in Reference [41]. The term with $B'(Q^2)$ contains the interference between the axial and vector currents, and it is this term which is responsible for the Q^2 dependent difference between the $\nu_\ell + n \rightarrow \ell^- + p$ and $\bar{\nu}_\ell + p \rightarrow \ell^+ + n$ cross sections. At $Q^2 = 0$, there is no difference between the CCQE cross sections for neutrinos and antineutrinos. Note that $s - u = 4ME_\nu - Q^2 - m_\ell^2$, where m_ℓ is the mass of the final state lepton; therefore,

the effect of the interference term is largest at small neutrino energies and high Q^2 .

In this analysis we use the published flux-averaged neutrino and antineutrino CCQE cross section results on hydrocarbon targets from the MINER ν A [15, 16] and MiniBooNE [11, 17] experiments. The results used are differential in terms of Q_{QE}^2 , derived from lepton kinematics under the quasielastic hypothesis,

$$Q_{\text{QE}}^2 = -m_\mu^2 + 2E_\nu^{\text{QE, FG}}(E_\mu - \sqrt{E_\mu^2 - m_\mu^2 \cos \theta_\mu}),$$

$$E_\nu^{\text{QE, FG}} = \frac{2M_i' E_\mu - (M_i'^2 + m_\mu^2 - M_f^2)}{2(M_i' - E_\mu + \sqrt{E_\mu^2 - m_\mu^2 \cos \theta_\mu})}, \quad (2)$$

where E_μ is the muon energy, m_μ is the muon mass, M_i (M_f) is the initial (final) nucleon mass, and $M_i' = M_i - V$ where V is the effective binding energy. For both MiniBooNE datasets and for the MINER ν A neutrino dataset, $V = 34$ MeV; for the MINER ν A antineutrino dataset, $V = 30$ MeV.

There are three differences in the neutrino and antineutrino cross section measurements for CCQE-like processes on hydrocarbon, CH_N targets. Firstly, the neutrino and antineutrino cross sections are fundamentally different for free nucleons (see Equation). Secondly, the neutrino and antineutrino fluxes produced in the same beamline may be different [42, 43]. Finally, antineutrinos can interact with the free proton from the hydrogen as well as bound protons within the carbon nucleus, whereas neutrinos can only interact with bound neutrons. A direct measurement of nuclear effects in carbon could be made by

$$\frac{6\sigma_{\text{H}}^{\bar{\nu}}}{\sigma_{\text{C}}^{\bar{\nu}}} = \frac{[(6 + N)\tilde{\sigma}_{\text{CH}_N}^{\bar{\nu}} - 6\lambda(Q^2)\tilde{\sigma}_{\text{CH}}^{\bar{\nu}}]}{N\lambda(Q^2)\tilde{\sigma}_{\text{CH}_N}^{\bar{\nu}}}, \quad (3)$$

where σ denotes the flux-averaged cross section for interactions between the neutrino species in the superscript and the target in the subscript; $\tilde{\sigma}$ denotes a cross section per nucleon; the correction factor $\lambda(Q^2) = (d\sigma_p^{\bar{\nu}}/dQ^2)/(d\sigma_n^{\bar{\nu}}/dQ^2)$ corrects for the difference between the neutrino and antineutrino nucleon cross sections and fluxes and is shown in Figure 1.

The validity of Equation 3 rests on the assumption that the ratio of bound to free cross sections is the same for neutrino and antineutrino scattering. As discussed in the supplementary material, within the FG model in the GENIE event generator, this assumption is well founded, except near the upper kinematic boundary in Q^2 at fixed neutrino energy where the nuclear corrections are largest. In the higher energy MINER ν A data sample with limited forward acceptance, this is a non-issue. For the MiniBooNE data sets, however, the lowest energy contributions to the flux integrated cross-section for $Q^2 \gtrsim 0.5$ GeV 2 will be affected by this inequality.

Another complication of this analysis is that experi-

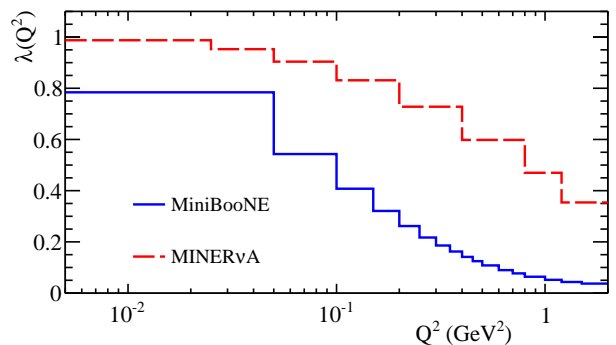


FIG. 1: $\lambda(Q^2) = \sigma_p^{\bar{\nu}}(Q^2)/\sigma_n^{\bar{\nu}}(Q^2)$ calculated using the free nucleon cross-sections implemented in the GENIE neutrino interaction generator [44], averaged over the relevant flux and binned into the Q^2 binning used by the relevant experiment. The values are given in the supplementary material.

ments measure differential cross-sections in Q_{QE}^2 , as defined in Equation 2, whereas the technique relates differential cross sections in Q^2 . The supplementary material shows the relationship between these two in the FG model. The differences are small compared to Q^2 bin widths for all relevant kinematics in the MINER ν A experiment; however, in MiniBooNE, the smearing becomes comparable to the bin width for $Q^2 > 0.2$ GeV 2 .

The measurement of nuclear effects on carbon is extracted from the public data releases for MINER ν A [15, 16][45] and MiniBooNE [11, 17] using Equation 3 with standard propagation of error techniques. For MINER ν A, the full covariance matrix, including cross-correlations, of the neutrino and antineutrino datasets is provided. For MiniBooNE, only the diagonals from the shape covariance matrices, and overall normalization factors are provided separately for the neutrino and antineutrino datasets (which we assume to be uncorrelated in this analysis). The data points and covariance matrices extracted in this work for both MINER ν A and MiniBooNE are available in the supplementary material.

Nuclear models available in the NEUT [46, 47] event generator are compared to the data. NEUT's default model is the Smith-Moniz [10] implementation of an FG model with Fermi momentum (p_F) and binding energy (E_b) on carbon set to $p_F = 217$ MeV and $E_b = 25$ MeV based on electron scattering data [48]. NEUT has implemented the Spectral Function (SF) model of Benhar [20, 49] which describes the initial nucleon's correlated momentum and removal energy and includes short range nuclear correlations which affect $\sim 20\%$ of the CCQE rate. Nuclear screening due to long-range nucleon correlations is implemented in RPA calculations [28]. Calculations of MNP use the model of Nieves *et al.* [28, 50]. NEUT also has implementations of two effective models constructed to ensure agreement with electron data, an

Effective Spectral Function (ESF) [23, 51, 52] and the Transverse Enhancement Model (TEM) [52, 53]. For all models, we use the BBBA05 vector nucleon form factors [54] and a dipole axial form factor with $M_A = 1.00$ GeV, based on fits to bubble chamber data [6–9]. These models span calculational approaches to nuclear models for CCQE in the literature, but are not a complete set. Another model can be compared to the measurements in this work using information in the supplementary material.

In Figure 2, the test statistic of Equation 3 is calculated, and compared with various combinations of the CCQE cross section models available in NEUT. A χ^2 value can be calculated for each model

$$\chi^2 = (\nu_i^{\text{DATA}} - \nu_i^{\text{MC}}) M_{ij}^{-1} (\nu_j^{\text{DATA}} - \nu_j^{\text{MC}}), \quad (4)$$

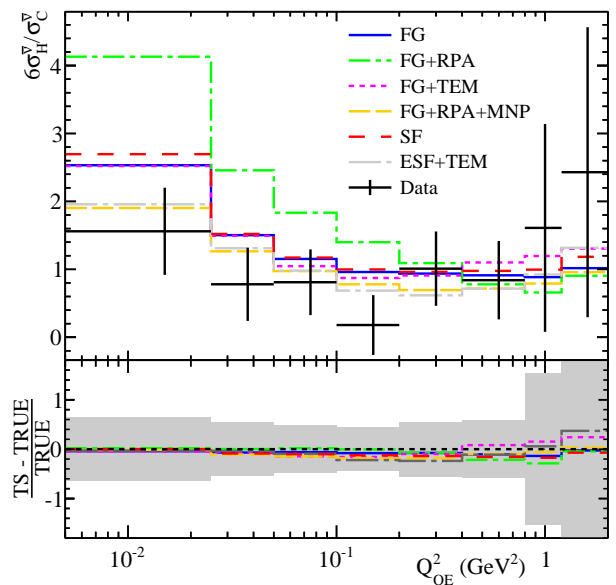
where the measurement of nuclear effects from data is given by ν_i^{DATA} , the covariance matrix between the data points is M_{ij} and the NEUT prediction for each model is given with ν_i^{MC} . The χ^2 values for each model are given for both MINER ν A and MiniBooNE in Table I.

Model	χ^2/DOF	
	MINER ν A	MiniBooNE
FG	14.8/8	6.0/17
FG+RPA	44.3/8	6.0/17
FG+RPA+MNP	13.6/8	6.8/17
FG+TEM	13.4/8	23.4/17
SF	15.9/8	6.1/17
ESF+TEM	12.8/8	6.2/17

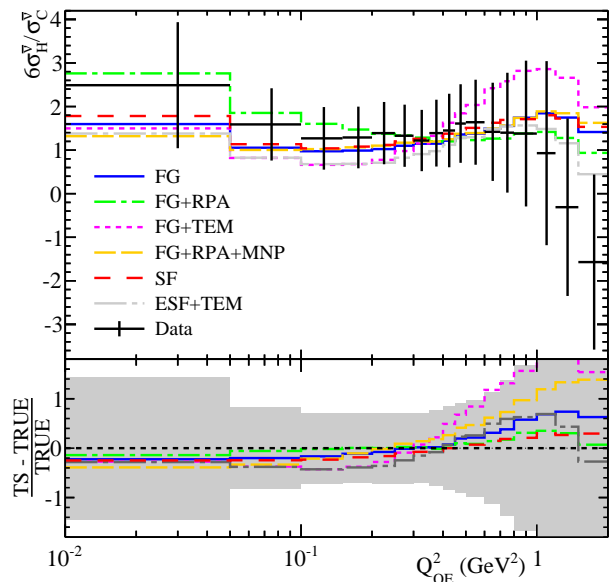
TABLE I: χ^2 values obtained with Equation 4 for the various cross section models shown in Figure 2.

Any model dependent bias in the test statistic due to the correction factor $\lambda(Q^2)$ or differences between Q_{QE}^2 and Q^2 can be calculated for each NEUT model by comparing the ratio $6\sigma_{\text{H}}^{\bar{\nu}}/\sigma_{\text{C}}^{\bar{\nu}}$ in that model (labeled TRUE) and to the test statistic (TS) calculated with Equation 3. A large deviation between the TS and TRUE values would indicate that the L-S $\lambda(Q^2)$ correction is inadequate to model the difference between the neutrino and antineutrino cross sections. Figure 2 shows that this deviation is small compared to fractional uncertainties on the test statistic measurement in data for MINER ν A, but that is it large for MiniBooNE.

The strong bias affecting the MiniBooNE measurement indicates that the $\lambda(Q^2)$ correction factor is inadequate for MiniBooNE. Likely this is because the MiniBooNE neutrino and antineutrino fluxes are very different at low energies, which is where the deficiencies in the model for bound nucleon cross sections are large due to kinematic limits. MINER ν A should be unaffected



(a) MINER ν A



(b) MiniBooNE

FIG. 2: The value of $6\sigma_{\text{H}}^{\bar{\nu}}/\sigma_{\text{C}}^{\bar{\nu}}$ calculated using Equation 3 is shown for a variety of NEUT models, as well as for the extracted MINER ν A and MiniBooNE data. The model dependent bias on $6\sigma_{\text{H}}^{\bar{\nu}}/\sigma_{\text{C}}^{\bar{\nu}}$ is quantified by comparing the value obtained with Equation 3 (TS) with the exact value calculated for each model (TRUE). The bias, $\frac{\text{TS}-\text{TRUE}}{\text{TRUE}}$, is compared with the fractional uncertainty on the measurement from data.

by this because the flux relevant for the measurement, $1.5 \leq E_{\nu} \leq 10$ GeV, places the kinematic limit at Q^2 beyond the range of this measurement. The higher energy flux also means that most MINER ν A (anti)neutrinos

could occupy any Q^2 bin, whereas much of the MiniBooNE flux ($0 \leq E_\nu \leq 3$ GeV) is kinematically limited to a subset of the Q_{QE}^2 bins investigated. This bias makes it difficult to meaningfully interpret the MiniBooNE result, and we will not consider it further.

We have treated the NEUT nuclear models as having no free parameters, and have calculated χ^2 values assuming nominal model parameters. Many of the models have no well defined theoretical uncertainties which can be varied in NEUT; however, the FG model does have a number of parameters which may be varied to estimate uncertainties within the base FG model, and we may additionally consider uncertainties in the axial form factor. To study this, we consider $M_A = 1.00 \pm 0.02$ GeV [6–9], $p_F = 217 \pm 5$ MeV [48], $E_b = 25 \pm 3$ MeV [48] and variations of 3 MeV in E_b for *either* neutrino or antineutrino to reflect uncertainty on whether the binding energy is the same for neutrons and protons. Additionally, we consider the 3% uncertainty on $F_P(0)$ recommended in Reference [41]; and take the difference between the non-dipole F_A from Reference [7] and the dipole F_A as a 1σ uncertainty. The uncertainties are combined in quadrature and compared to the fractional uncertainty on the data in Figure 3. The

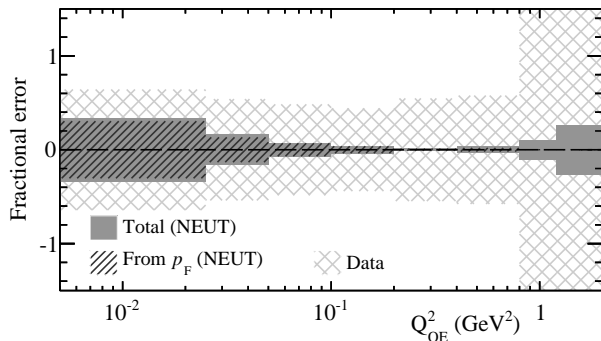


FIG. 3: The fractional uncertainty on the value of $6\sigma_H^\nu/\sigma_C^\nu$ calculated for the FG model with MINER ν A. The total uncertainty is obtained by combining the 1σ uncertainties in quadrature, and the dominant uncertainty, p_F is also shown separately. The fractional uncertainty on the data is shown for comparison.

FG model uncertainty is most significant at low Q^2 and is dominated by the uncertainty on the Fermi momentum, p_F . As the model bias of our measurement is smallest at low Q^2 , changing p_F may improve the χ^2 between our measurement and the predictions of the various FG based models considered in this work. We extend the χ^2 calculation from Equation 4 to include a variable p_F parameter with a penalty term based on the p_F uncertainty from electron-scattering data [48]. The best fit χ^2 and p_F result for each of the FG based models is shown in Table II for MINER ν A. The fit reduces p_F slightly in order to reduce the value of $6\sigma_H^\nu/\sigma_C^\nu$ at low Q_{QE}^2 , but there is no significant improvement in fit quality.

Model	χ^2/DOF		p_F (GeV 2)
	Nominal	Fit	
FG	14.8	14.1	213.8 ± 4.0
FG+RPA	44.3	38.2	207.6 ± 4.0
FG+RPA+MNP	13.6	13.5	214.1 ± 3.9
FG+TEM	13.4	12.8	215.8 ± 4.5

TABLE II: Best fit χ^2 and p_F results for the fit to FG based models for MINER ν A data. The nominal χ^2 with $p_F = 217$ MeV is included for comparison.

In this analysis, a method for measuring the nuclear effects of carbon ($6\sigma_H^\nu/\sigma_C^\nu$) using cross section data on hydrocarbon targets has been defined, and results extracted from published MINER ν A and MiniBooNE CCQE cross section data. The method exploits the fact that antineutrinos have additional interactions on free protons (from the hydrogen), and corrects for neutrino and antineutrino flux and cross section differences. We find that the method works well for MINER ν A data, and the model dependent bias is small for all nuclear models tested. We provide full information in the supplementary material to allow tests of the model dependence of our method for any nuclear model. The extracted measurement of nuclear effects in carbon is the first of its kind, and is easy to interpret for model builders. The strongest conclusion is that models with only an RPA suppression at low Q^2 fare poorly without addition of MNP to balance the RPA, and models with both are weakly favored over a plain FG model. Constraints from this method could be improved using future, higher statistics, MINER ν A CCQE measurements. The method does not work well for MiniBooNE data due to large flux differences between the MiniBooNE neutrino and antineutrino in the low energy region. This analysis could be repeated for cross section measurements in terms of different kinematic variables, although a high Q^2 bias will remain.

This work was supported by the United States Department of Energy under Grant DE-SC0008475 and by the Swiss National Science Foundation and SERI. CW is grateful to the University of Rochester for hospitality while this work was being carried out. We thank Geryl Zeller for useful discussions about this technique during its early development, and in particular for information about MiniBooNE’s consideration of a similar analysis. We thank the developers of the NEUT generator for implementation of many alternate nuclear models, and the T2K collaboration for supporting this development. We thank the MINER ν A collaboration for early release of their data corrected for the improved flux simulation.

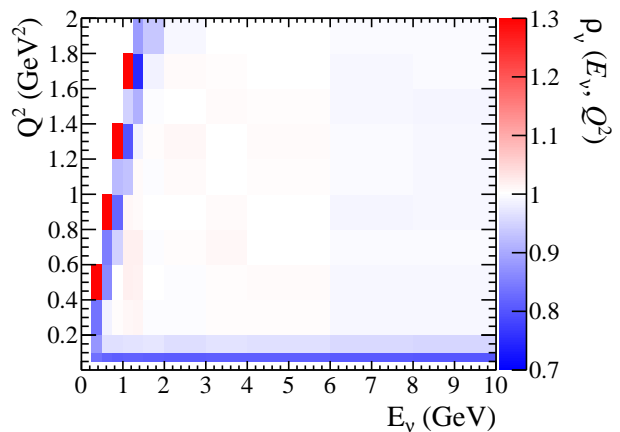
- [1] S. L. Adler, *Il Nuovo Cimento* (1955-1965) **30**, 1020 (1963).
- [2] R. E. Marshak, Riazuddin, and C. P. Ryan, *Theory of Weak Interactions in Particle Physics* (Wiley-Interscience, 1969) pp. 1–761.
- [3] A. Pais, *Annals Phys.* **63**, 361 (1971).
- [4] C. Llewellyn Smith, *Phys. Rept.* **3**, 261 (1972).
- [5] H. S. Budd, A. Bodek, and J. Arrington.
- [6] K. S. Kuzmin, V. V. Lyubushkin, and V. A. Naumov, *Acta Phys. Polon.* **B37**, 2337 (2006), arXiv:hep-ph/0606184 [hep-ph].
- [7] A. Bodek, S. Avvakumov, R. Bradford, and H. Budd, *The European Physical Journal C* **53**, 349 ().
- [8] K. S. Kuzmin, V. V. Lyubushkin, and V. A. Naumov, *Eur. Phys. J.* **C54**, 517 (2008), arXiv:0712.4384 [hep-ph].
- [9] A. Bodek, S. Avvakumov, R. Bradford, and H. S. Budd, *J. Phys. Conf. Ser.* **110**, 082004 (2008), arXiv:0709.3538 [hep-ex].
- [10] R. Smith and E. Moniz, *Nucl. Phys.* **B43**, 605 (1972).
- [11] A. Aguilar-Arevalo *et al.* (MiniBooNE Collaboration), *Phys. Rev.* **D81**, 092005 (2010), arXiv:1002.2680 [hep-ex].
- [12] R. Gran *et al.* (K2K), *Phys. Rev.* **D74**, 052002 (2006), arXiv:hep-ex/0603034 [hep-ex].
- [13] V. Lyubushkin *et al.*, *The European Physical Journal C* **63**, 355 (2009).
- [14] M. Dorman (MINOS Collaboration), *AIP Conf. Proc.* **1189**, 133 (2009).
- [15] G. Fiorentini *et al.* (MINER ν A Collaboration), *Phys. Rev. Lett.* **111**, 022502 (2013), arXiv:1305.2243 [hep-ex].
- [16] L. Fields *et al.* (MINER ν A Collaboration), *Phys. Rev. Lett.* **111**, 022501 (2013), arXiv:1305.2234 [hep-ex].
- [17] A. Aguilar-Arevalo *et al.* (MiniBooNE Collaboration), *Phys. Rev.* **D88**, 032001 (2013), arXiv:1301.7067 [hep-ex].
- [18] K. Abe *et al.* (T2K), *Phys. Rev.* **D91**, 112002 (2015), arXiv:1503.07452 [hep-ex].
- [19] K. Abe *et al.* (T2K), *Phys. Rev.* **D92**, 112003 (2015), arXiv:1411.6264 [hep-ex].
- [20] O. Benhar and A. Fabrocini, *Phys. Rev.* **C62**, 034304 (2000), arXiv:nucl-th/9909014 [nucl-th].
- [21] A. M. Ankowski and J. T. Sobczyk, *Phys. Rev. C* **74**, 054316 (2006).
- [22] A. Butkevich, *Phys. Rev.* **C80**, 014610 (2009), arXiv:0904.1472 [nucl-th].
- [23] A. Bodek, M. Christy, and B. Coopersmith, *Eur. Phys. J.* **C74**, 3091 (2014), arXiv:1405.0583 [hep-ph].
- [24] T. Leitner, O. Buss, L. Alvarez-Ruso, and U. Mosel, *Phys. Rev. C* **79**, 034601 (2009).
- [25] C. Maieron, M. Martinez, J. Caballero, and J. Udias, *Phys. Rev.* **C68**, 048501 (2003), arXiv:nucl-th/0303075 [nucl-th].
- [26] A. Meucci, C. Giusti, and F. D. Pacati, *Nucl. Phys.* **A739**, 277 (2004), arXiv:nucl-th/0311081 [nucl-th].
- [27] V. Pandey, N. Jachowicz, T. Van Cuyck, J. Ryckebusch, and M. Martini, *Phys. Rev.* **C92**, 024606 (2015), arXiv:1412.4624 [nucl-th].
- [28] J. Nieves, I. R. Simo, and M. J. V. Vacas, *Phys. Rev. C* **83**, 045501 (2011).
- [29] M. Martini, M. Ericson, G. Chanfray, and J. Marteau, *Phys. Rev.* **C80**, 065501 (2009), arXiv:0910.2622 [nucl-th].
- [30] J. A. Formaggio and G. P. Zeller, *Rev. Mod. Phys.* **84**, 1307 (2012).
- [31] L. Alvarez-Ruso, Y. Hayato, and J. Nieves, *New J. Phys.* **16**, 075015 (2014), arXiv:1403.2673 [hep-ph].
- [32] G. T. Garvey, D. A. Harris, H. A. Tanaka, R. Tayloe, and G. P. Zeller, *Phys. Rept.* **580**, 1 (2015), arXiv:1412.4294 [hep-ex].
- [33] A. Aguilar-Arevalo *et al.* (MiniBooNE Collaboration), *Phys. Rev. Lett.* **102**, 101802 (2009), arXiv:0812.2243 [hep-ex].
- [34] K. Abe *et al.* (T2K Collaboration), *Phys. Rev. Lett.* **107**, 041801 (2011).
- [35] D. Ayres *et al.*, (2005), available at hep-ex/0503053v1.
- [36] K. Abe, T. Abe, H. Aihara, Y. Fukuda, Y. Hayato, *et al.*, (2011), arXiv:1109.3262 [hep-ex].
- [37] R. Acciarri *et al.* (DUNE), (2016), arXiv:1601.05471 [physics].
- [38] M. Martini, M. Ericson, and G. Chanfray, *Phys. Rev.* **D87**, 013009 (2013), arXiv:1211.1523 [hep-ph].
- [39] O. Lalakulich and U. Mosel, *Phys. Rev.* **C86**, 054606 (2012), arXiv:1208.3678 [nucl-th].
- [40] J. Nieves, F. Sanchez, I. R. Simo, and M. J. V. Vacas, *Phys. Rev.* **D85**, 113008 (2012), arXiv:1204.5404 [hep-ph].
- [41] M. Day and K. S. McFarland, *Phys. Rev.* **D86**, 053003 (2012), arXiv:1206.6745 [hep-ph].
- [42] S. E. Kopp, (2005), arXiv:physics/0508001 [physics].
- [43] A. Aguilar-Arevalo *et al.* (MiniBooNE Collaboration), *Phys. Rev.* **D79**, 072002 (2009), arXiv:0806.1449 [hep-ex].
- [44] C. Andreopoulos, A. Bell, D. Bhattacharya, F. Cavanna, J. Dobson, *et al.*, *Nucl. Instrum. Meth.* **A614**, 87 (2010), arXiv:0905.2517 [hep-ph].
- [45] The results used here correspond to the results with a flux estimate [55] updated from the original publication, which predicts a significantly smaller flux and a smaller fractional flux uncertainty.
- [46] Y. Hayato, *Acta Physica Polonica B* **40**, 2477 (2009).
- [47] C. Wilkinson *et al.*, (2016), arXiv:1601.05592 [hep-ex].
- [48] E. J. Moniz, I. Sick, R. R. Whitney, J. R. Ficenc, R. D. Kephart, and W. P. Trower, *Phys. Rev. Lett.* **26**, 445 (1971).
- [49] A. Furmanski, *Charged-current Quasi-elastic-like neutrino interactions at the T2K experiment*, Ph.D. thesis, University of Warwick (2015).
- [50] R. Gran, J. Nieves, F. Sanchez, and M. Vicente Vacas, *Phys. Rev.* **D88**, 113007 (2013), arXiv:1307.8105 [hep-ph].
- [51] A. Bodek, M. E. Christy, and B. Coopersmith.
- [52] C. Wilkinson, *Constraining neutrino interaction uncertainties for oscillation experiments*, Ph.D. thesis, University of Sheffield (2015).
- [53] A. Bodek, H. S. Budd, and E. Christy, *Eur. Phys. J. C* **71**, 1726 (2011).
- [54] R. Bradford, A. Bodek, H. Budd, and J. Arrington, *Nuclear Physics B - Proceedings Supplements* **159**, 127 (2006).
- [55] L. Aliaga, M. Kordosky, T. Golan, *et al.* (MINER ν A Collaboration), “Private communication of manuscript in preparation, prediction of the numi neutrino flux,” (2016).

APPENDIX: EQUALITY OF THE NUCLEAR CORRECTION FOR NEUTRINOS AND ANTINEUTRINOS IN THE FERMI GAS MODEL

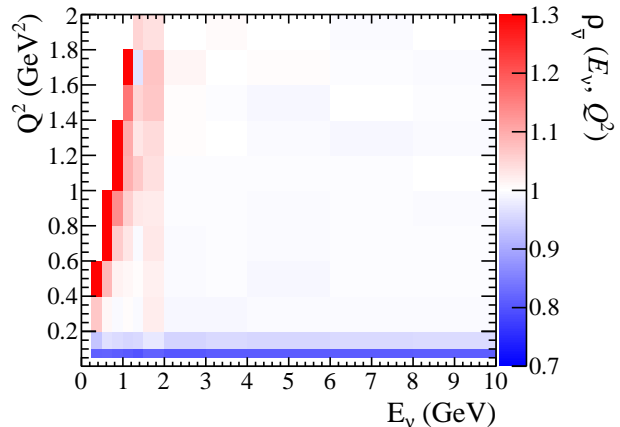
The validity of Equation 3 rests on the assumption that the ratio of bound to free cross sections is the same for neutrino and antineutrino modes. Figure 4 shows the ratio of bound to free CCQE cross sections for both neutrino ($\rho_\nu(E_\nu, Q^2) = \sigma_\nu^{\text{RFG}}(E_\nu, Q^2)/\sigma_\nu^{\text{free}}(E_\nu, Q^2)$) and antineutrinos ($\rho_{\bar{\nu}}(E_\nu, Q^2) = \sigma_{\bar{\nu}}^{\text{RFG}}(E_\nu, Q^2)/\sigma_{\bar{\nu}}^{\text{free}}(E_\nu, Q^2)$) assuming the RFG model in GENIE for bound nucleons as a function of E_ν and Q^2 . The simulated events used to produce Figure 4 are flat in neutrino energy. In Figure 5, the double ratio

$$\xi(E_\nu, Q^2) = \frac{\sigma_\nu^{\text{RFG}}(E_\nu, Q^2)/\sigma_\nu^{\text{free}}(E_\nu, Q^2)}{\sigma_{\bar{\nu}}^{\text{RFG}}(E_\nu, Q^2)/\sigma_{\bar{\nu}}^{\text{free}}(E_\nu, Q^2)} \quad (5)$$

is shown, which is a direct test of this assumption for the case of the RFG model. It can be observed from Figure 4 that at the fringe of the kinematically allowed region, where Fermi motion increases the allowed phase space for the RFG model, the ratio of bound to free cross sections changes rapidly. It is clear from Figure 5 that this change is different for neutrino and antineutrino modes. This implies that there will be a bias in the test statistic defined in Equation 3 for neutrino energies which cannot populate all Q^2 bins. MINER ν A, where the flux has neutrino energies in the range $1.5 \leq E_\nu \leq 10$ GeV, will not be affected by the bias. However, MiniBooNE, with neutrino energies of $0 \leq E_\nu \leq 3$ GeV, will be affected, although the size of this bias on the test statistic is not clear from Figure 5. The biases are shown for both MINER ν A and MiniBooNE in Figure 2.



(a) Neutrino



(b) Antineutrino

FIG. 4: Ratios of $\sigma(E_\nu, Q^2)$ for the RFG and L-S models, for both neutrino and antineutrino modes.

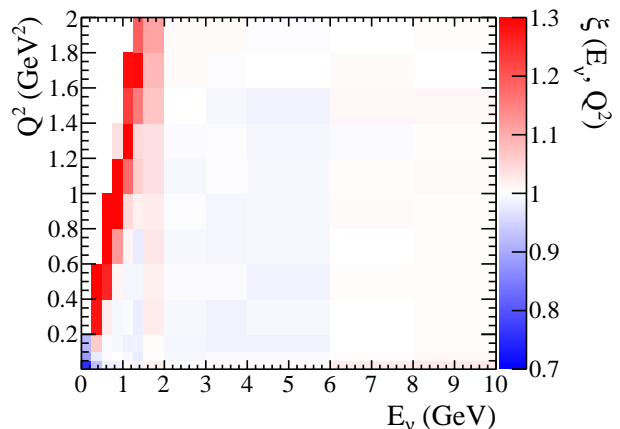
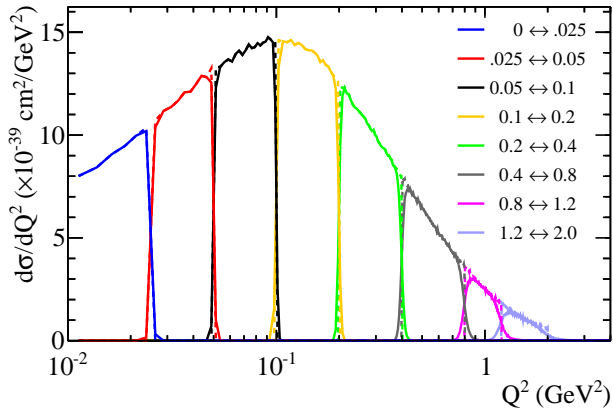
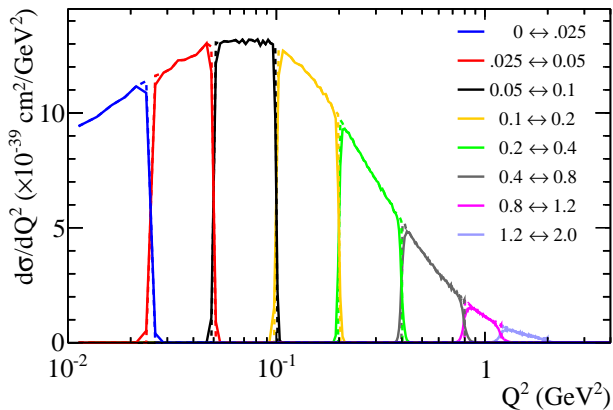


FIG. 5: The double ratio $\xi(E_\nu, Q^2)$, defined in Equation 5, is shown. Deviations from unity indicates a bias in the technique in that region of (E_ν, Q^2) space.

APPENDIX: RELATIONSHIP BETWEEN
MEASURED Q_{QE}^2 AND Q^2



(a) MINERνA ν_μ -CH

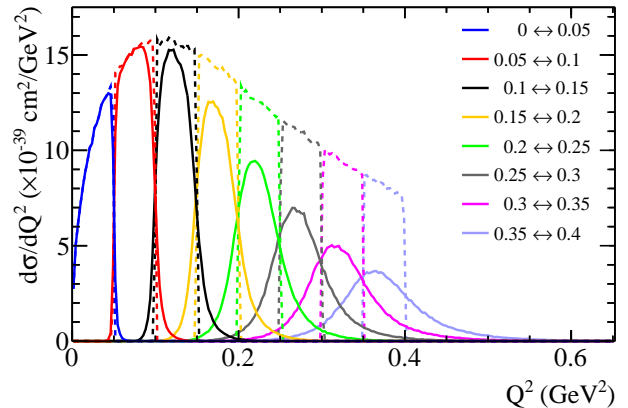


(b) MINERνA $\bar{\nu}_\mu$ -CH

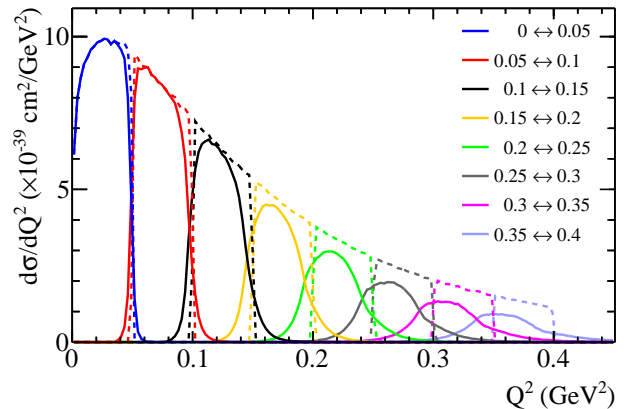
FIG. 6: The $Q^2 \rightarrow Q_{QE}^2$ smearing is shown for the MINERνA neutrino and antineutrino samples. The legend gives the Q_{QE}^2 bin edges used by MINERνA. The dashed lines give the flux-averaged cross section prediction for the FG model calculated using NEUT as a function of Q_{QE}^2 (broken down into the MINERνA binning). The solid lines show the true Q^2 distribution of events in each Q_{QE}^2 bin.

The $Q^2 \rightarrow Q_{QE}^2$ effect for the FG model is illustrated in Figure 6 for MINERνA, and Figure 7 for MiniBooNE. In both figures, the true Q^2 distribution is shown for events which populate each of the first 8 Q_{QE}^2 bins of the experiments using events simulated using the FG model in NEUT with default model parameters. The smearing is not very significant for MINERνA, and is minimal in the lowest Q_{QE}^2 bins. For MiniBooNE, the smearing becomes significant in the higher Q_{QE}^2 bins (and this trend continues for the other bins not shown in Figure 7), but is minimal at low Q_{QE}^2 . Q_{QE}^2 is effectively an additional smearing effect on the Q^2 distribution measured by the experiments, which is dependent on the nuclear model.

As such it is part of the measurement of nuclear effects, but it will smear the bias introduced by correcting for the antineutrino/neutrino cross section difference with the L-S model. This effect is not corrected for, but is included in the bias tests shown on Figure 2. Again, it is reassuring that the Q_{QE}^2 smearing is minimal at low Q^2 .



(a) MiniBooNE ν_μ -CH₂



(b) MiniBooNE $\bar{\nu}_\mu$ -CH₂

FIG. 7: The $Q^2 \rightarrow Q_{QE}^2$ smearing is shown for the first 8 bins of the MiniBooNE neutrino and antineutrino samples. The legend gives the Q_{QE}^2 bin edges used by MiniBooNE. The dashed lines give the flux-averaged cross section prediction for the FG model calculated using NEUT as a function of Q_{QE}^2 (broken down into the MiniBooNE binning). The solid lines show the true Q^2 distribution of events in each Q_{QE}^2 bin.

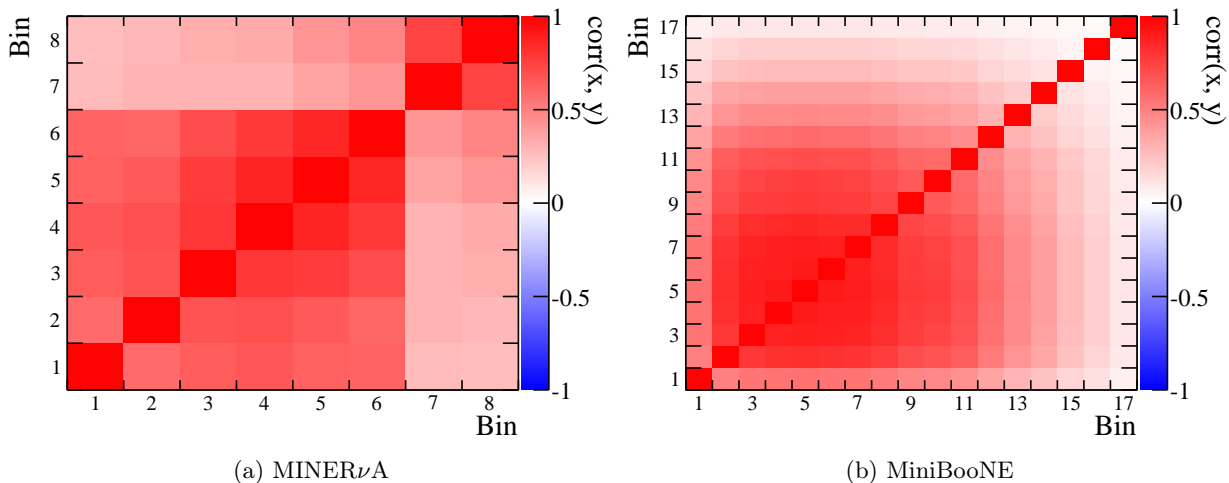


FIG. 8: Correlation matrices between the measurement of the test statistic extracted from data for both MINERνA and MiniBooNE. The bins numbers correspond to the increasing Q_{QE}^2 bins used by the experiments. The covariance matrices are given in Tables III and IV for MINERνA and MiniBooNE respectively.

Q_{QE}^2 (GeV ²) bins	0 – 0.025	0.025 – 0.05	0.05 – 0.1	0.1 – 0.2	0.2 – 0.4	0.4 – 0.8	0.8 – 1.2	1.2 – 2
Test statistic	1.61	0.83	0.85	0.22	1.06	0.89	1.66	2.49
$\lambda(Q^2)$	0.988	0.953	0.904	0.831	0.728	0.598	0.470	0.354
0 – 0.025	0.439	0.213	0.212	0.197	0.233	0.254	0.293	0.389
0.025 – 0.05	0.213	0.306	0.186	0.172	0.204	0.210	0.275	0.356
0.05 – 0.1	0.212	0.186	0.244	0.177	0.216	0.217	0.242	0.356
0.1 – 0.2	0.197	0.172	0.177	0.201	0.218	0.219	0.221	0.331
0.2 – 0.4	0.233	0.204	0.216	0.218	0.318	0.302	0.330	0.532
0.4 – 0.8	0.254	0.210	0.217	0.219	0.302	0.388	0.423	0.677
0.8 – 1.2	0.293	0.275	0.242	0.221	0.330	0.423	2.619	2.699
1.2 – 2	0.389	0.356	0.356	0.331	0.532	0.677	2.699	4.947

TABLE III: The measurement of nuclear effects on carbon using MINERνA data on CH , calculated using Equation 3, and the covariance matrix between the data points.

APPENDIX: APPLYING THE METHOD TO AN ARBITRARY THEORETICAL MODEL

The extracted central values, $\lambda(Q^2) = \sigma_p^{\bar{\nu}}(Q^2)/\sigma_n^{\nu}(Q^2)$ correction factors and covariance matrices are given for MINERνA and MiniBooNE in Tables III and IV respectively. The extracted correlation matrices are also shown for both MINERνA and MiniBooNE in Figure 8. Note that no covariance matrix between the MiniBooNE bins has been released for either the neutrino or the antineutrino CCQE results; the correlations shown are due to the overall normalization uncertainties given independently

for the neutrino (10.7%) and antineutrino (13.0%) data which are fully correlated between bins (but are not correlated with each other).

It is possible to apply the method outlined here to any cross section model using Equation 3, using the $\lambda(Q^2)$ correction factor. As shown in Figure 2, the bias on the test statistic can be shown for any given model by calculating $6\sigma_H^{\bar{\nu}}/\sigma_C^{\bar{\nu}}$ using the test statistic defined in this work, and exactly using that model.

It is possible to form a χ^2 statistic comparing an arbitrary model to the measurements of nuclear effects extracted here as described in Equation 4.

Q_{QE}^2 (GeV ²) bins	0	0.05	0.1	0.1	0.15	0.15	0.2	0.2	0.25	0.25	0.3	0.3	0.35	0.35	0.4	0.4	0.4	0.45	0.45	0.5	0.5	0.5	0.6	0.6	0.7	0.7	0.8	0.8	1	1	1.2	1.2	1.5	1.5	2
Test statistic	2.49	1.59	1.27	1.29	1.39	1.39	1.33	1.22	1.39	1.45	1.61	1.64	1.42	1.4	1.38	0.93	-0.31	-1.57																	
$\lambda(Q^2)$	0.784	0.543	0.408	0.321	0.262	0.262	0.217	0.186	0.162	0.141	0.125	0.108	0.090	0.077	0.064	0.052	0.043	0.037																	
0 - 0.05	2.093	0.609	0.568	0.570	0.583	0.583	0.574	0.561	0.583	0.591	0.613	0.616	0.587	0.585	0.582	0.522	0.358	0.190																	
0.05 - 0.1	0.609	0.688	0.475	0.477	0.487	0.487	0.480	0.469	0.487	0.495	0.512	0.515	0.491	0.489	0.486	0.436	0.299	0.158																	
0.1 - 0.15	0.568	0.475	0.516	0.444	0.454	0.447	0.447	0.437	0.454	0.461	0.477	0.480	0.457	0.455	0.453	0.407	0.279	0.148																	
0.15 - 0.2	0.570	0.477	0.444	0.501	0.456	0.449	0.449	0.439	0.456	0.463	0.479	0.482	0.459	0.457	0.455	0.408	0.280	0.148																	
0.2 - 0.25	0.583	0.487	0.454	0.456	0.511	0.459	0.459	0.449	0.466	0.473	0.490	0.493	0.469	0.468	0.465	0.417	0.286	0.152																	
0.25 - 0.3	0.574	0.480	0.447	0.449	0.459	0.509	0.442	0.459	0.466	0.466	0.483	0.486	0.463	0.461	0.458	0.411	0.282	0.149																	
0.3 - 0.35	0.561	0.469	0.437	0.439	0.449	0.442	0.495	0.449	0.449	0.455	0.471	0.474	0.452	0.450	0.448	0.402	0.275	0.146																	
0.35 - 0.4	0.583	0.487	0.454	0.456	0.466	0.459	0.459	0.449	0.466	0.473	0.490	0.493	0.469	0.467	0.465	0.417	0.286	0.152																	
0.4 - 0.45	0.591	0.495	0.461	0.463	0.473	0.466	0.466	0.455	0.473	0.472	0.497	0.500	0.476	0.474	0.472	0.424	0.290	0.154																	
0.45 - 0.5	0.613	0.512	0.477	0.479	0.490	0.483	0.483	0.471	0.490	0.497	0.813	0.518	0.493	0.491	0.489	0.439	0.301	0.159																	
0.5 - 0.6	0.616	0.515	0.480	0.482	0.493	0.486	0.486	0.474	0.493	0.500	0.518	0.952	0.496	0.494	0.492	0.441	0.302	0.160																	
0.6 - 0.7	0.587	0.491	0.457	0.459	0.469	0.463	0.463	0.452	0.469	0.476	0.493	0.496	1.270	0.471	0.468	0.420	0.288	0.153																	
0.7 - 0.8	0.585	0.489	0.455	0.457	0.468	0.461	0.461	0.450	0.467	0.474	0.491	0.494	0.471	1.892	0.466	0.419	0.287	0.152																	
0.8 - 1	0.582	0.486	0.453	0.455	0.465	0.458	0.458	0.448	0.465	0.472	0.489	0.492	0.468	0.466	2.800	0.416	0.285	0.151																	
1 - 1.2	0.522	0.436	0.407	0.408	0.417	0.411	0.402	0.402	0.417	0.424	0.439	0.441	0.420	0.419	0.416	4.462	0.256	0.136																	
1.2 - 1.5	0.358	0.299	0.279	0.280	0.286	0.282	0.282	0.275	0.286	0.290	0.301	0.302	0.288	0.287	0.285	0.256	4.152	0.093																	
1.5 - 2	0.190	0.158	0.148	0.148	0.152	0.149	0.146	0.146	0.152	0.154	0.159	0.160	0.153	0.152	0.151	0.136	0.093	4.036																	

TABLE IV: The measurement of nuclear effects on carbon using MiniBooNE data on CH_2 , calculated using Equation 3, and the covariance matrix between the data points.